

## Research Article

# Effect of Fe Doping on Photocatalytic Dye-Degradation and Antibacterial Activity of SnO<sub>2</sub> Nanoparticles

T. Preethi <sup>1</sup>, K. Senthil <sup>2</sup>, M. P. Pachamuthu <sup>3</sup>, R. Balakrishnaraja <sup>4</sup>, B. Sundaravel <sup>5</sup>,  
N. Geetha <sup>6</sup>, and Stefano Bellucci <sup>7</sup>

<sup>1</sup>Advanced Materials Research Laboratory, Department of Physics, Bannari Amman Institute of Technology, Sathyamangalam, Tamil Nadu 638401, India

<sup>2</sup>Department of Physics, School of Advanced Sciences, VIT-AP University, Amaravati, Andhra Pradesh 522237, India

<sup>3</sup>Integrated AI & Sensors Lab, Department of Chemistry, Bannari Amman Institute of Technology, Sathyamangalam, Tamil Nadu 638401, India

<sup>4</sup>Department of Biotechnology, Bannari Amman Institute of Technology, Sathyamangalam, Tamil Nadu 638401, India

<sup>5</sup>Materials Science Group, Indira Gandhi Centre for Atomic Research, HBNI, Kalpakkam, Tamil Nadu 603102, India

<sup>6</sup>Department of Zoology (PG), PSG College of Arts & Science, Coimbatore, Tamil Nadu 641014, India

<sup>7</sup>INFN-Laboratori Nazionali di Frascati, 00044 Frascati, Italy

Correspondence should be addressed to K. Senthil; [ksenthiludt@gmail.com](mailto:ksenthiludt@gmail.com) and M. P. Pachamuthu; [pachamuthu@bitsathy.ac.in](mailto:pachamuthu@bitsathy.ac.in)

Received 27 February 2022; Revised 21 March 2022; Accepted 11 April 2022; Published 9 May 2022

Academic Editor: George Kyzas

Copyright © 2022 T. Preethi et al. This is an open access article distributed under the Creative Commons Attribution License, which permits unrestricted use, distribution, and reproduction in any medium, provided the original work is properly cited.

A simple hydrothermal method is utilized to synthesize iron-doped tin oxide nanoparticles (Fe-SnO<sub>2</sub> NPs) at various doping concentrations. The structural characterization using XRD, Raman, and FTIR measurements confirmed the incorporation of Fe ions into the SnO<sub>2</sub> lattice without any deviation in the tetragonal crystal system of SnO<sub>2</sub> nanoparticles. SEM and HRTEM images show the spherical-shaped nanoparticles with agglomeration. The values of interplanar spacing (*d*-value) calculated from the HRTEM lattice are consistent with the XRD results. Further, optical analysis revealed a red shift in the optical absorption band and a decrease in the band gap energy with an increase in Fe-dopant concentration. The decrease of PL emission peak intensity with Fe doping revealed the generation of singly charged oxygen vacancies. The H<sub>2</sub>O<sub>2</sub>-assisted photocatalytic degradation efficiency of Fe-SnO<sub>2</sub> NPs investigated against crystal violet dye indicated an efficiency of 98% for 0.05 M Fe-SnO<sub>2</sub> NPs within 30 minutes under visible light illumination. In addition, the effects of pH, scavengers, and reusability of the catalyst are tested. The antibacterial behavior of Fe-SnO<sub>2</sub> NPs against *Escherichia coli* is examined by using the colony count method, and the inhibition rate was found to be 49, 65, 70, and 78% for pure, 0.01, 0.03, and 0.05 M Fe-SnO<sub>2</sub> NPs, respectively.

## 1. Introduction

Globally, the release of effluents into the environment has been increased due to rapid industrialization, which may cause adverse effects on the ecological and aquatic environment. Dyes are a major source of pollution since they are utilized in a variety of sectors, including food, cosmetics, plastic, leather, paper, and textiles. The presence of complex aromatic structures in the dyes makes them difficult to degrade, which may cause color changes, odor changes, excessive nutrients, biocontamination, and underoxygena-

tion in the aquatic environment [1, 2]. Therefore, it is highly essential to remove these contaminants from wastewater to achieve a concentration below the level accepted for environmentally safe disposal. Adsorption [3–5], biodegradation [6], photocatalysis [7, 8], ultrasound-assisted method [9], and ozonation [10] are the procedures used to remove these contaminants from wastewater. Among these methods, considerable attention has been paid on photocatalytic degradation due to its ability to produce highly reactive radicals for efficient removal of contaminants [11]. Semiconducting metal oxide nanoparticles, especially SnO<sub>2</sub>, have gained

significant attention due to their unique properties such as good photochemical stability, high oxidizing power, cost effectiveness, and environment friendly nature [12]. Although it has several advantages, the main drawback of using SnO<sub>2</sub> nanoparticles for photocatalytic degradation is faster recombination rate of electron-hole pairs. The promising solution to overcome this problem is to introduce a metal dopant into the SnO<sub>2</sub> lattice, which will increase the visible light absorption ability by decreasing the band gap of SnO<sub>2</sub>. Baig et al. observed that doping SnO<sub>2</sub> nanoparticles with Zn and Y increased their photocatalytic efficiency towards methylene blue [13, 14]. Sathishkumar and Geethalakshmi have reported the synthesis of Cu:SnO<sub>2</sub> nanoparticles with improved antibacterial and photocatalytic activity under ultraviolet light [15]. Ragupathy and Sathya have shown Ni doping in SnO<sub>2</sub> nanoparticles by chemical precipitation method for increasing the photocatalytic degradation of brilliant green dye to a considerable extent [16]. The effect of Fe doping and surfactant on the photocatalytic behavior of SnO<sub>2</sub> nanoparticles is studied by Sujatha et al. [17]. Among the various transition metal atoms, Fe seems to be a suitable dopant. The presence of half-filled electronic structure in Fe tends to narrow down the band gap by forming new intermediate energy levels, and electron-hole pair recombination rate is minimized by the trapped photogenerated electrons [18, 19]. Hence, in this study, pure and Fe-SnO<sub>2</sub> NPs are synthesized at various Fe concentrations (0.01, 0.03, and 0.05 M) by using a simple surfactant-free hydrothermal technique. The structure, surface morphology, composition, optical, photocatalytic dye-degradation, and antibacterial properties are investigated systematically. The investigations revealed an enhancement in the photocatalytic degradation efficiency and antibacterial activity with increasing Fe-dopant concentration.

## 2. Experimental Procedures

**2.1. Fe-SnO<sub>2</sub> Nanoparticle Synthesis.** Tin (IV) chloride pentahydrate (SnCl<sub>4</sub>·5H<sub>2</sub>O) and ferric chloride hexahydrate (FeCl<sub>3</sub>·6H<sub>2</sub>O) are used as metal precursors; sodium hydroxide (NaOH) is used as a precipitating agent; methyl alcohol (CH<sub>3</sub>OH) and double deionized water are used for washing of the obtained precipitates. Double-distilled water is used as a solvent for all the synthesis process. All the chemicals are utilized with no further purification. SnCl<sub>4</sub>·5H<sub>2</sub>O (0.4 M) and FeCl<sub>3</sub>·6H<sub>2</sub>O at various concentrations (0.01, 0.03, and 0.05 M) are dissolved in 50 mL of double-deionized water in a conventional synthesis. The pH of precursor solution was adjusted to 10 by adding NaOH solution, and final solution is agitated at room temperature for 30 min. The contents are then transferred to an autoclave and hydrothermally treated for 24 h at 150°C. After the completion of reaction, the autoclave is allowed to cool down to room temperature. To eliminate unreacted chemicals, the precipitate is centrifuged and washed many times with double-distilled water and methyl alcohol. Final solid is dehydrated for 12 h at 80°C and heated for 3 h at 600°C.

**2.2. Characterization Techniques.** The crystalline structures of Fe-SnO<sub>2</sub> NPs are analyzed using an X-ray diffractometer (Inel Equinox 2000). WITec Alpha 300 Raman spectrometer is used for Raman and photoluminescence measurements at different excitation wavelengths 532 and 355 nm, respectively. A Fourier transform infrared spectrophotometer [Shimadzu-Japan 00719 (A221355)] is used to screen the surface functional groups of the nanoparticles. A scanning electron microscope (SEM-Leo 440i) is used to examine the surface morphology and composition. A high-resolution transmission electron microscope (JEM-2100 Plus, JEOL-Japan) is employed to obtain the lattice images and SAED patterns. The optical absorption spectra are recorded using a UV-visible spectrophotometer (Edinburgh Instruments FLS 980) with Xenon lamp as a light source.

**2.3. Photocatalytic Dye-Degradation and Antibacterial Activity.** The catalytic activity of the Fe-SnO<sub>2</sub> samples are investigated by monitoring the decomposition of dye in the presence of H<sub>2</sub>O<sub>2</sub> under visible light illumination using 125 W mercury vapour lamp. The degradation efficiency is investigated by analysing the absorption maximum of the dye by using a UV-visible spectrophotometer (Shimadzu UV 1800). Antibacterial activity of the synthesized samples is investigated by using colony count method against gram-negative *Escherichia coli* bacterial strain.

## 3. Results and Discussion

**3.1. XRD Analysis.** The XRD diffraction patterns of synthesized pure and Fe-SnO<sub>2</sub> NPs at different concentrations (0.01, 0.03, and 0.05 M) are shown in Figure 1. The XRD peaks detected in the XRD pattern of pure samples (Figure 1(a)) correspond well to the standard JCPDS data # 41-1445, confirming the formation of a tetragonal crystalline structure. The peaks observed at 26.50°, 33.89°, 37.85°, 51.74°, 54.70°, 57.72°, 61.73°, 64.74°, 65.92°, and 71.25° correspond to the crystal planes (110), (101), (200), (211), (220), (002), (310), (112), (301), and (202), respectively. The XRD patterns of Fe-SnO<sub>2</sub> NPs are identical to those of pure SnO<sub>2</sub> NPs, with a modest shift in peak position and a reduction in the intensity. The decrease in peak intensity as the Fe-dopant concentration increases suggests that dopant ions have been incorporated into the SnO<sub>2</sub> lattice effectively. The observed shift in peak positions is due to the substitution of Fe ions with smaller ionic radii (0.063 nm) in the site of Sn (0.069 nm) [17]. Besides, the XRD patterns do not reveal any other impurities or secondary-phase peaks, indicating that the synthesized samples are in pure crystalline form. The calculated mean crystalline sizes of the particles are found to be 9.38, 4.48, 4.88, and 4.87 nm for pure and (0.01, 0.03, and 0.05 M) Fe-SnO<sub>2</sub> NPs, respectively. The strain generated by Fe-dopant ions in the host lattice can be attributed to the reduction in crystalline size for the Fe-doped samples. Baig et al., Segueni et al., and Rao et al. reported the similar results for Fe-SnO<sub>2</sub> samples [19–21].

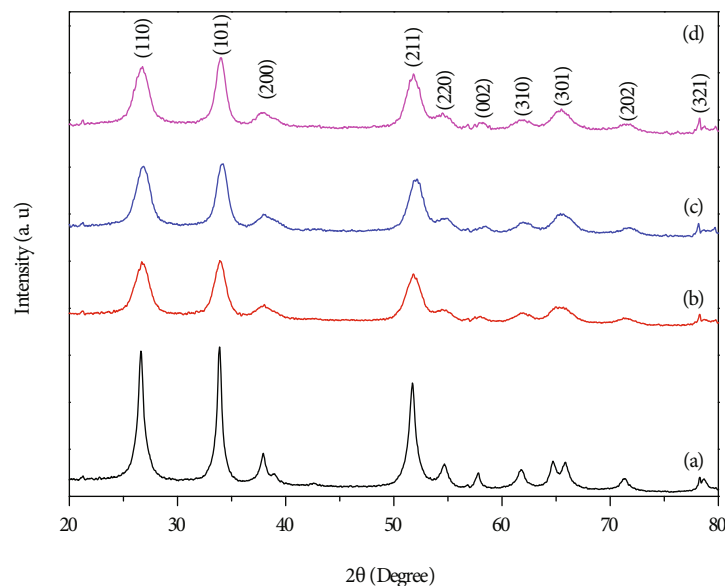


FIGURE 1: XRD patterns of (a) pure, (b) 0.01 M, (c) 0.03 M, and (d) 0.05 M Fe-SnO<sub>2</sub> NPs.

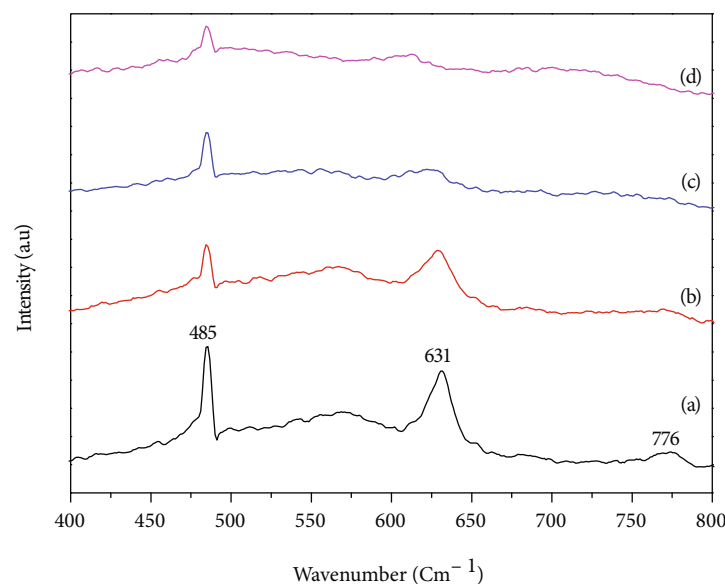


FIGURE 2: Raman spectra of (a) pure, (b) 0.01 M, (c) 0.03 M, and (d) 0.05 M Fe-SnO<sub>2</sub> NPs.

**3.2. Raman Analysis.** The typical vibrational modes of the Brillouin zone of SnO<sub>2</sub> are represented by using group theory [22].

$$\Gamma = A_{1g} + A_{2g} + B_{1g} + B_{2g} + E_g + 2A_{2u} + 2B_{1u} + 4E_u. \quad (1)$$

The Raman modes  $B_{1g}$ ,  $E_g$ ,  $A_{1g}$ , and  $B_{2g}$  observed at wavenumbers 123, 473, 634, and 773 cm<sup>-1</sup>, respectively, are active and caused by the vibration of oxygen atoms when Sn atoms are not in vibration. The Raman spectra (Figure 2(a)) of pure SnO<sub>2</sub> NPs exhibit three active modes at 485, 631, and 776 cm<sup>-1</sup> related to  $E_g$ ,  $A_{1g}$ , and  $B_{2g}$  vibrations, respectively [23]. The modes  $A_{1g}$  (631 cm<sup>-1</sup>) and  $B_{2g}$  (776 cm<sup>-1</sup>) are

caused by asymmetric stretching of Sn-O, but the mode  $E_g$  (485 cm<sup>-1</sup>) is caused by the vibration of two oxygen atoms along the  $c$ -axis but in the reverse direction, and it is highly susceptible to oxygen vacancies. In addition, the presence of three fundamental Raman modes confirms the formation of tetragonal rutile structure in SnO<sub>2</sub> NPs. From the Raman spectra of Fe-SnO<sub>2</sub> NPs (Figures 2(b)–2(d)), it is observed that the intensity of  $E_g$ ,  $A_{1g}$ , and  $B_{2g}$  mode diminishes on increasing the Fe-dopant concentration, and the  $B_{2g}$  mode observed at 776 cm<sup>-1</sup> is completely vanished at 0.05 M Fe-SnO<sub>2</sub> NPs. This supports the XRD results by indicating that Fe ions are integrated into the SnO<sub>2</sub> lattice. The similar observation of a decrease in peak intensity of the  $B_{2g}$  mode

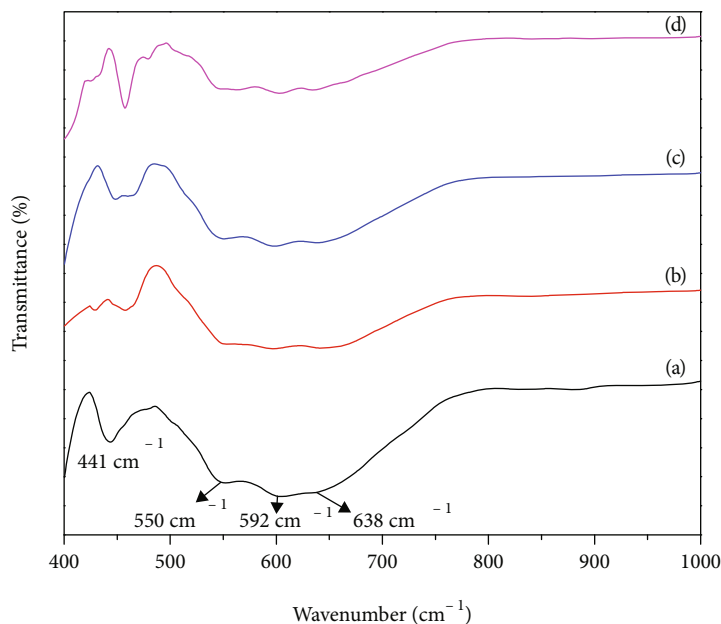


FIGURE 3: FTIR spectra of (a) pure, (b) 0.01 M, (c) 0.03 M, and (d) 0.05 M Fe-SnO<sub>2</sub> NPs.

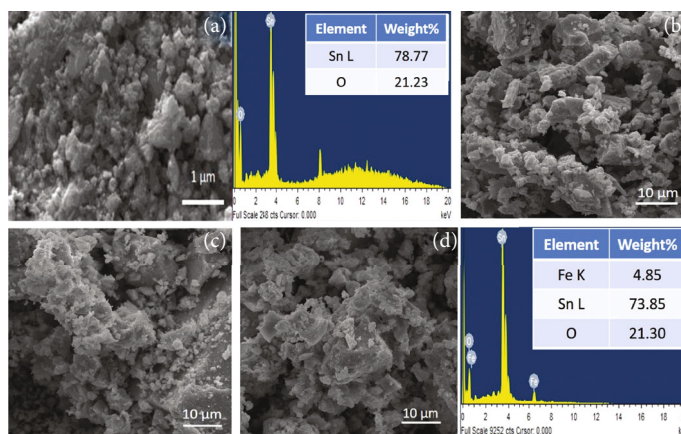


FIGURE 4: SEM micrographs of (a) pure, (b) 0.01 M, (c) 0.03 M, and (d) 0.05 M Fe-SnO<sub>2</sub> NPs and EDS spectra of pure and 0.05 M Fe-SnO<sub>2</sub> NPs.

has been observed by Jayapandi et al. [24] and Othmen et al. [25] for La-doped and Fe-doped SnO<sub>2</sub> NPs, respectively.

**3.3. FTIR Analysis.** The bonding nature of the synthesized Fe-SnO<sub>2</sub> nanoparticles was identified by FTIR and displayed in Figure 3. The major peak appearing in the region of 441-445 cm<sup>-1</sup> can be associated with the stretching mode of O-Sn-O bonding [26]. Remarkably, this stretching mode is shifted towards higher wavenumber (~450 cm<sup>-1</sup>) when the dopant concentration is increased. The vibrational bands appearing in the regions 550-557 cm<sup>-1</sup> and 592-598 cm<sup>-1</sup> were ascribed to Sn-O and Sn-O-Sn stretching vibrations, respectively [27, 28]. Further, the peak found in all samples around 638-642 cm<sup>-1</sup> could be related to the O-Sn-O functional group, which confirmed the formation of SnO<sub>2</sub> NPs [17].

**3.4. Morphology and Elemental Composition Analysis.** Figure 4 shows the morphological structure and elemental composition of the Fe-SnO<sub>2</sub> nanoparticles studied with SEM and EDS analysis, respectively. The SEM micrograph obtained from pure SnO<sub>2</sub> sample (Figure 4(a)) indicates the irregular distribution of particles which are agglomerated. With increasing Fe-dopant concentration, the agglomeration rate increases further (Figures 4(b)-4(d)), and this increase in agglomeration is mainly attributed to the higher surface free energy and larger surface area of the nanoparticles which have the tendency to agglomerate because of the stronger attractive forces exhibited by the surface atoms. The presence of Sn, O, and Fe as important trace elements were confirmed by EDS spectra corresponding to Figures 4(a) and 4(d). The calculated weight percent of the observed elements is shown in the EDS spectra inset tables.

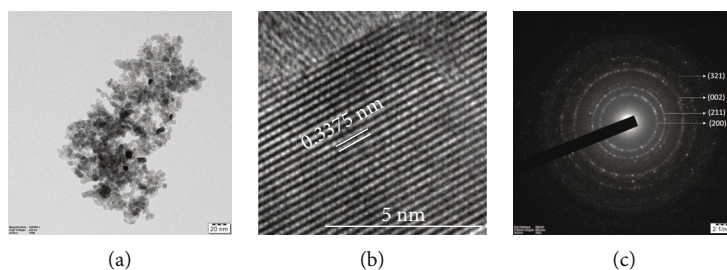


FIGURE 5: (a) HRTEM image, (b) HRTEM lattice image, and (c) SAED pattern obtained from the 0.05 M Fe-SnO<sub>2</sub> NPs.

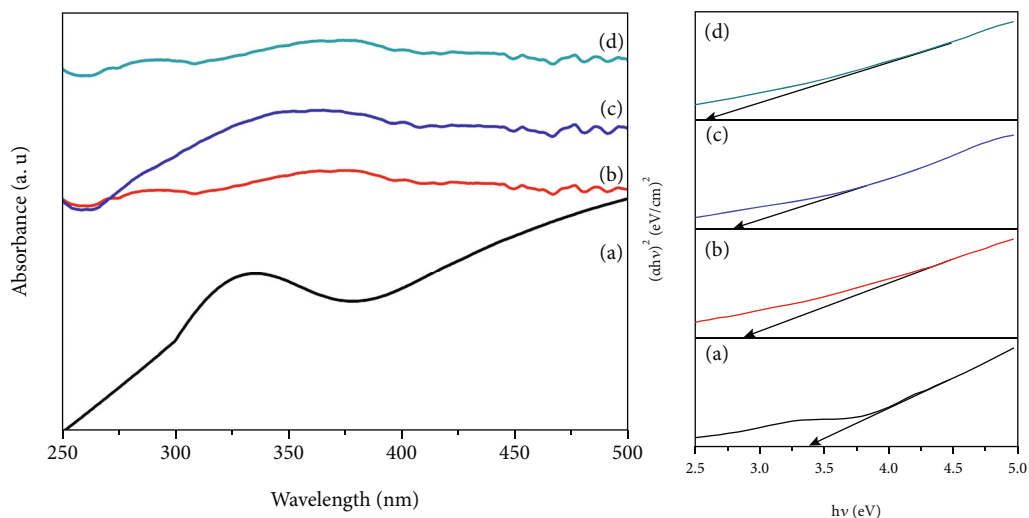


FIGURE 6: Optical absorption spectra and Tauc's plot of (a) pure, (b) 0.01 M, (c) 0.03 M, and (d) 0.05 M Fe-SnO<sub>2</sub> NPs.

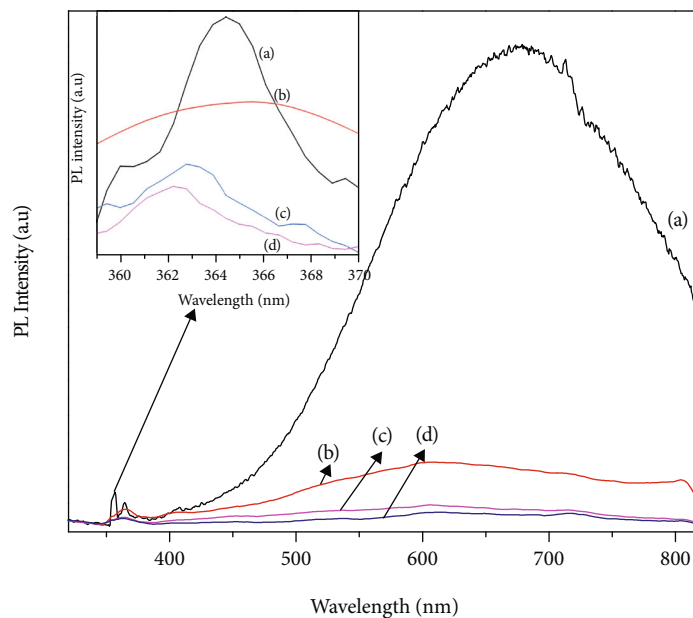
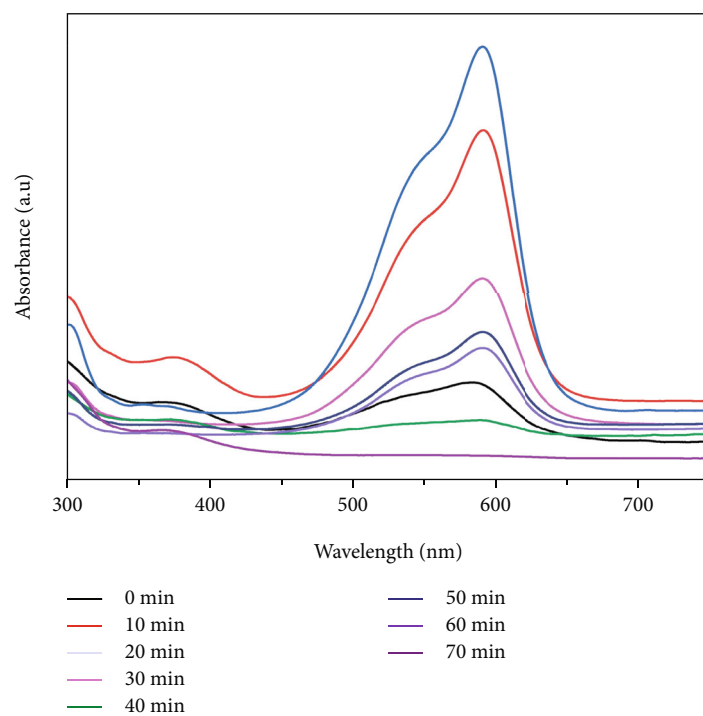


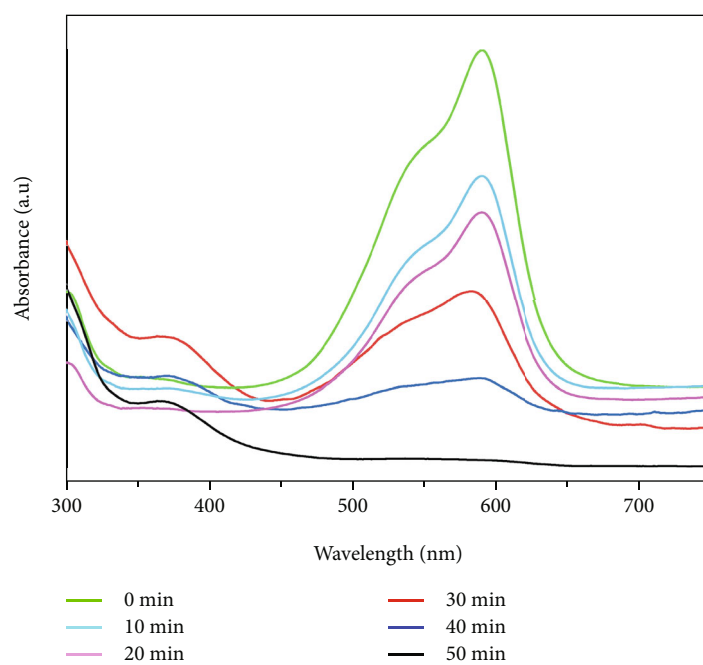
FIGURE 7: PL spectra of (a) pure, (b) 0.01 M, (c) 0.03 M, and (d) 0.05 M Fe-SnO<sub>2</sub> NPs.

3.5. HRTEM and SAED Analysis. The formation of spherical shaped nanoparticles with agglomeration was observed in the HRTEM image (Figure 5(a)) of the 0.05 M Fe-SnO<sub>2</sub>

NPs sample. The interplanar spacing ( $d_{hkl}$ ) is calculated from the HRTEM lattice image shown in Figure 5(b). In addition, the calculated value of  $d_{hkl}$  (0.3375 nm) is almost

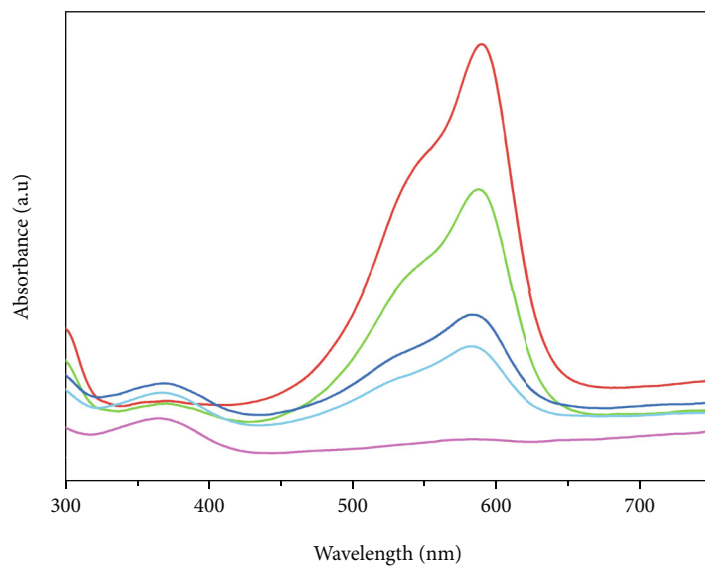


(a)



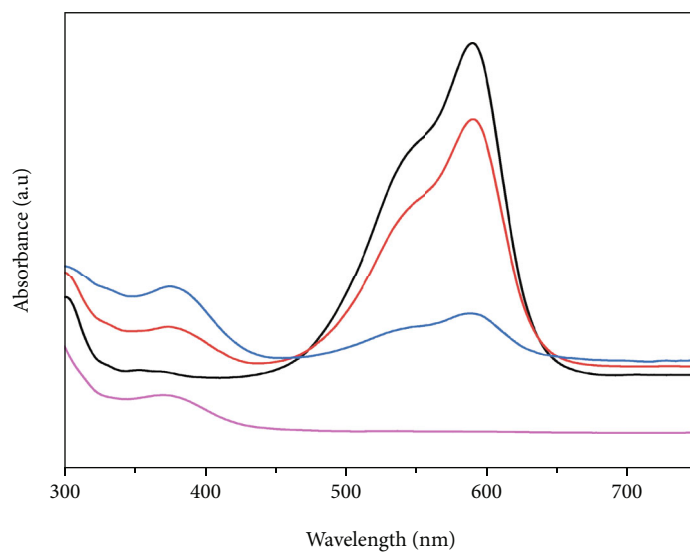
(b)

FIGURE 8: Continued.



- 0 min
- 10 min
- 20 min
- 30 min
- 40 min

(c)



- 0 min
- 10 min
- 20 min
- 30 min

(d)

FIGURE 8: Continued.

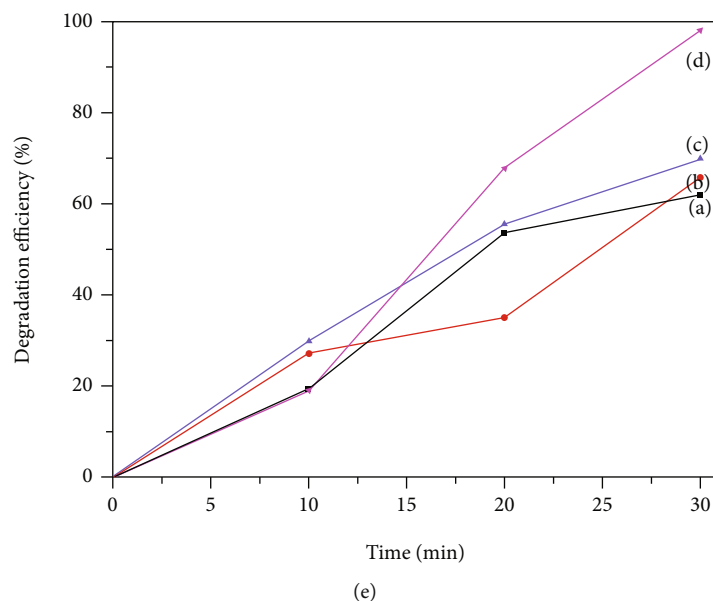


FIGURE 8: Optical absorption spectra depicting the degradation of crystal violet dye using (a) pure, (b) 0.01 M, (c) 0.03 M, (d) 0.05 M Fe-SnO<sub>2</sub> NPs, and (e) efficiency vs. time graph.

very close to the values obtained from the XRD data (0.3359 nm) and JCPDS data (0.3347 nm). Notably, the SAED pattern (Figure 5(c)) indicates the polycrystalline nature of the synthesized Fe-SnO<sub>2</sub> NPs and having tetragonal crystal structure.

**3.6. UV-Visible Absorption Spectroscopy.** Figure 6 shows the UV-visible absorption spectra in the 250–500 nm wavelength region. In the near-UV range, the optical absorption spectrum of pure SnO<sub>2</sub> NPs revealed a broad absorption band. With increasing Fe-dopant level, a red shift in the absorption band has been observed, and this shift in the absorption band provides a proof for the integration of dopants in the host lattice. The Tauc's plots presented in Figure 6 were used to estimate the values of band gap. The estimated values are 3.36, 2.85, 2.77, and 2.58 eV for pure, 0.01, 0.03, and 0.05 M Fe-SnO<sub>2</sub> NPs, respectively. Further, the vacancies or defects due to the absence of oxygen created by the Fe dopants in the host are responsible for the blue shift noticed in band gap energy. The quantum confinement effect cannot be treated as the reason for band gap reduction, since the crystallite size reduction does not increase the band gap here. Thus, the oxygen vacancies are considered as the sole reason for the band gap reduction in the present work [29].

**3.7. Photoluminescence Spectroscopy.** The recorded photoluminescence spectra are shown in Figure 7. In the spectra, there are two peaks: a weak band ( $\approx 359$  nm) and a strong band ( $\approx 650$  nm) are noticed. The photogenerated electron-hole pairs undergo radiative recombination, resulting in weak band emission. The electrons in the deep level energy states undergo radiative recombination, and the holes generated in the valence band due to photoexcitation produce electrons in deep level states. The photoexcited holes in the

valence band produce a strong emission in the visible region. Further, the intensity of PL emission peak decreases on increasing the Fe concentration, which is indicating the trapping of electron-hole pairs by oxygen vacancies, and leads to the creation of singly ionized oxygen vacancies with the accumulation of Fe<sup>+</sup> ions [19]. The lower the intensity of PL emission peak, the lower will be the electron-hole recombination rate, which is favorable for photocatalytic activity, and hence, it is expected that the 0.05 M Fe-SnO<sub>2</sub> NPs sample will give efficient results towards the degradation of dye molecules when compared to other samples.

**3.8. Photocatalytic Dye Degradation.** The photocatalytic efficiency of Fe-SnO<sub>2</sub> NPs to degrade crystal violet dye is performed by using H<sub>2</sub>O<sub>2</sub>-assisted photocatalytic process. H<sub>2</sub>O<sub>2</sub> is a well-known photooxidant in waste water treatment since it creates hydroxyl radicals that degrade harmful pollutants when illuminated with visible light, hence enhancing the photocatalytic efficacy [12]. Initially, a required ppm of CV dye solution is prepared, and then, the certain amount of Fe-SnO<sub>2</sub> sample (20 mg) is added to the dye solution, and 30 minutes of stirring is done to achieve equilibrium in adsorption-desorption process. Under continuous stirring, an appropriate amount of H<sub>2</sub>O<sub>2</sub> (0.5 mL) is added into the dye solution under visible light irradiation. The dye degradation efficiency of the synthesized nanoparticles is elucidated by measuring the absorbance using UV-visible spectrophotometer at regular intervals. Figures 8(a)–8(d) show the absorption spectra taken at regular time intervals during the crystal violet dye-degradation using pure and 0.01 M, 0.03 M, and 0.05 M Fe-SnO<sub>2</sub> NPs, respectively. It is observed that the intensity of characteristic absorption peak corresponding to crystal violet decreases slowly with increasing time, and the degradation is noticed clearly from the variation in the dye color.

TABLE 1: Comparison of catalytic dye degradation efficiency of the present work with the previously reported literature.

Material	Dye	Light source	Efficiency (%)	Time (min)	Reference
Fe:SnO <sub>2</sub>			43		
Fe:SnO <sub>2</sub> (CTAB)	Methylene blue	Visible light (500 W)	25	120	Ref [17]
Fe:SnO <sub>2</sub> (SDS)			28		
Fe:SnO <sub>2</sub> (Triton)			49		
Fe:TiO <sub>2</sub>	Methyl orange	Visible light (250 W)	69		Ref [18]
Fe:SnO <sub>2</sub>		Visible light (500 W)	87.2	200	Ref [19]
Ni:SnO <sub>2</sub>	Brilliant green	Sunlight	97.54	105	Ref [16]
Fe:SnO <sub>2</sub>	Crystal violet	Visible light (125 W) + H <sub>2</sub> O <sub>2</sub>	98.23	30	Present work

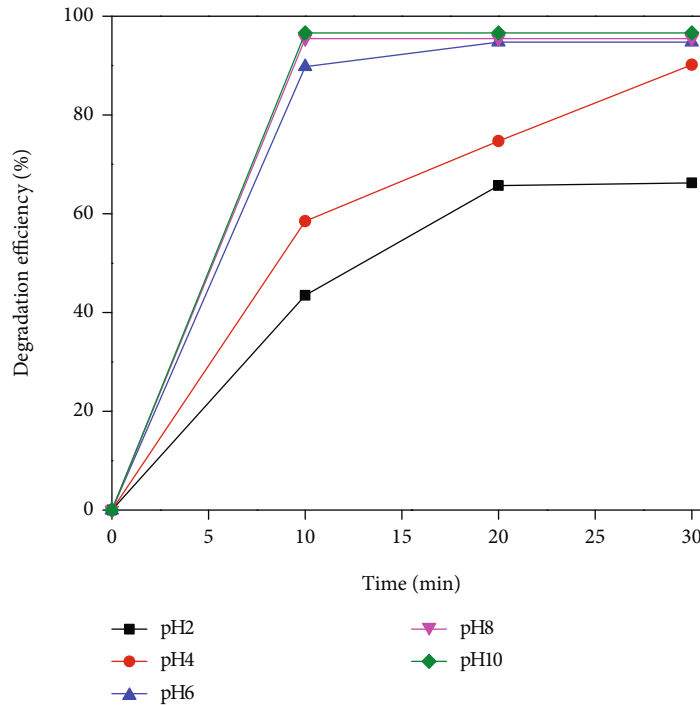


FIGURE 9: Effect of different radical scavengers on degradation of crystal violet dye.

With increasing dopant concentration, the degradation time reduces monotonically. The crystal violet dye was completely degraded after 30 minutes of light illumination for the 0.05 M Fe-SnO<sub>2</sub> NPs, which could be due to the efficient separation of electron-hole pairs as the dopant concentration is increased, as evidenced by the PL analysis, which showed reduced PL intensity with increasing Fe-dopant concentration, implying a lower electron-hole recombination rate. The efficiency of degradation is computed from the following equation reported in [30].

$$\text{Degradation Efficiency} = \left[ 1 - \frac{A}{A_0} \right] \times 100. \quad (2)$$

The degradation efficiency vs. time curves of the pure and Fe-SnO<sub>2</sub> NPs are shown in Figure 8(e). For 0.05 M Fe-SnO<sub>2</sub> NPs, a maximum degradation efficiency of 98% is observed

in 30 minutes. To study the role of light source in degradation process, a blank test is carried out without using the light source for 0.05 M Fe-doped SnO<sub>2</sub> sample, and the result showed only 7% degradation efficiency in 30 minutes. From this result, it is clear that the synthesized Fe-SnO<sub>2</sub> NPs acts as efficient photocatalyst in the presence of both H<sub>2</sub>O<sub>2</sub> and light source. Thus, we have successfully synthesized Fe-SnO<sub>2</sub> NPs having 98% efficiency to degrade crystal violet dye within 30 min of visible light irradiation even in the presence of less catalyst (20 mg) and H<sub>2</sub>O<sub>2</sub> (0.5 mL), whereas the other literature reported low efficiency even after longer irradiation time. A detailed comparison of the results obtained in the present work is compared with previously reported literatures and tabulated in Table 1. These comparisons revealed that the photocatalyst efficiency to degrade dye molecules can be increased by adding H<sub>2</sub>O<sub>2</sub>. In general, the mechanism behind the photocatalytic dye degradation process can be explained as follows.

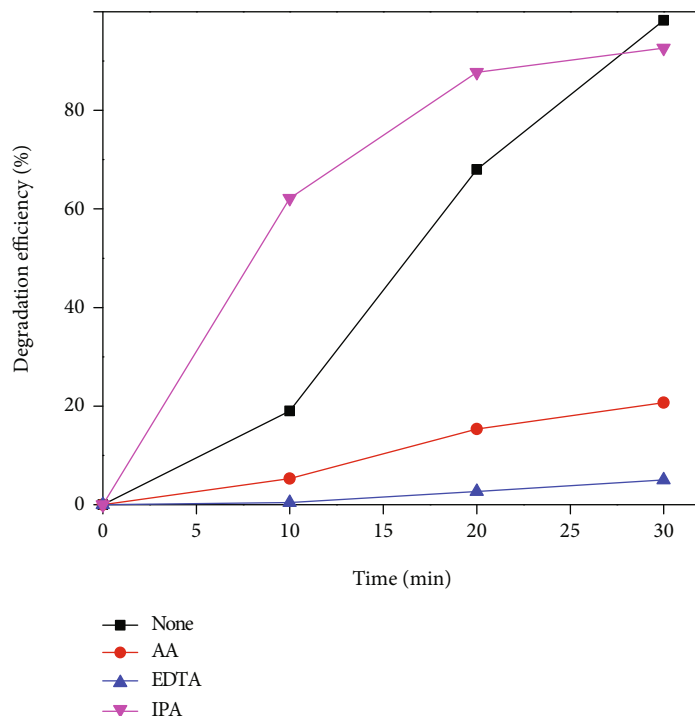
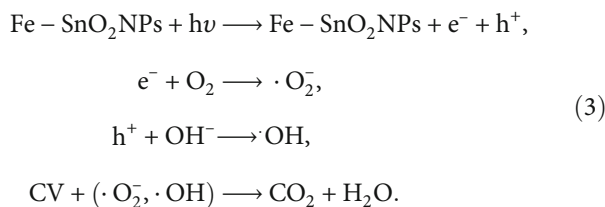


FIGURE 10: Effect of pH on the degradation of crystal violet dye using 0.05 M Fe-SnO<sub>2</sub> NPs.

When a photon with energy higher than the band gap excites the photocatalyst, the electrons are elevated into the conduction band from the valence band, and holes are generated. These generated electrons form superoxide radicals by reacting with dissolved oxygen, whereas the produced holes transform OH<sup>-</sup> into ·OH radicals. The mechanism can be described by using the following equations:



H<sub>2</sub>O<sub>2</sub> has played an important role in the photocatalytic reaction because it acts as an electron acceptor, absorbing photon energy, and forming hydroxyl radicals. As a result, the probability of electron-hole recombination rate will be reduced. The produced superoxide radical anions and hydroxyl radicals are expected to be responsible to break-down the dye molecules [31].

**3.8.1. Effect of Scavengers on Degradation Efficiency.** In order to identify the active species which govern the degradation process, the reaction is carried out in the presence of 0.5 mM ethylene diamine tetra acetic acid (EDTA), isopropyl alcohol (IPA), and ascorbic acid (AA) as holes (h<sup>+</sup>), hydroxyl radical (·OH), and superoxide radical anions (·O<sub>2</sub><sup>-</sup>) scavengers, respectively. Figure 9 shows the degradation efficiency of Fe-SnO<sub>2</sub> NPs while using different scavengers, and the results suggest that efficiency is in the order of

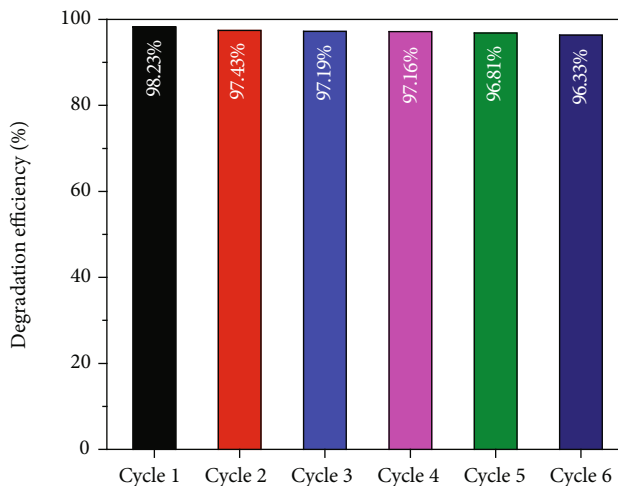


FIGURE 11: Recycling ability and stability of 0.05 M Fe-SnO<sub>2</sub> nanoparticles.

No scavengers > IPA > AA > EDTA. The very feeble role of hydroxyl radical in degradation process is identified from the slight reduction in efficiency while using hydroxyl radical scavenger (IPA). The minimum degradation efficiency of 5% and 21% is observed while using EDTA and AA, respectively. This strongly indicates that the holes and superoxide radical anions play a significant role in the degradation of crystal violet dye.

**3.8.2. Effect of pH on Degradation of Crystal Violet Dye.** The degradation efficiency of nanoparticles depends on pH of the dye solution, since it controls the production of hydroxyl

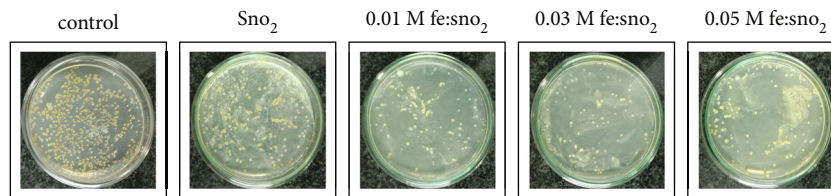


FIGURE 12: Antibacterial potential of pure and Fe-SnO<sub>2</sub> NPs.

radicals during the degradation process. To study the effect of pH, we have varied the pH of dye solution from 2 to 10 by using 1 M NaOH and HCl solutions. After adjusting the pH, the dye solution containing an appropriate amount of 0.05 M Fe-doped SnO<sub>2</sub> nanoparticles is stirred for 30 min in dark to obtain an equilibrium between the catalyst and dye molecules. In this stage, H<sub>2</sub>O<sub>2</sub> (0.5 mL) is added and stirred continuously under visible light illumination. UV-visible absorption spectra were taken at regular time interval to study its degradation efficiency. The degradation efficiency increases while increasing the pH of dye solution as shown in Figure 10, and the results clearly indicated a maximum degradation efficiency of 98% for the nanoparticles in the basic medium (pH = 10). In the basic medium, the charge on the surface of Fe-doped SnO<sub>2</sub> nanoparticles tends to be negative which attracts the cationic crystal violet dye via electrostatic force of attraction [2].

**3.8.3. Reusability and Stability of Fe-SnO<sub>2</sub> NPs.** It is important to study the reusability and stability of the catalyst to identify its practical applicability. The catalyst was collected and dried after each cycle and was reused for the next cycle. Figure 11 indicates that the Fe-doped SnO<sub>2</sub> nanoparticles showed only a slight variation in degradation efficiency of crystal violet dye from 98% to 96% after five cycles. This result confirms that the synthesized Fe-doped SnO<sub>2</sub> nanoparticles are stable when reused.

**3.9. Antibacterial Activity.** Antibacterial activity of the synthesized pure and Fe-SnO<sub>2</sub> NPs against *Escherichia coli* was studied by using colony count method. This method is particularly advantageous when the nanoparticle suspension offers less diffusion through the medium. In this method, bacterial strains are grown in a nutrient broth medium overnight at a temperature of 37°C in an orbital shaker. Further, the number of colony forming unit (CFU) is adjusted to  $1 \times 10^2$  cells/mL by using a 75 mM saline solution. 100  $\mu$ L of the above medium is spread on the nutrient agar plates using L-rod, and same quantity of the aqueous nanoparticle suspension is also spread over the bacterium inoculated plates and incubated at 37°C for 24 h. Here, the plates without the nanoparticle suspension is used as a control. The number of colonies formed is counted, and the percentage of inhibition is found by using the formula

$$\% \text{Inhibition} = \frac{(\text{Control} - \text{Test})}{\text{Test}} * 100. \quad (4)$$

The obtained antibacterial activity of pure and Fe-SnO<sub>2</sub> NPs at different concentrations is depicted in Figure 12.

The inhibition rate of pure, 0.01 M, 0.03 M, and 0.05 M Fe-SnO<sub>2</sub> NPs against gram-negative bacteria *Escherichia coli* is found to be 49, 65, 70, and 78%, respectively. Notably, the observed inhibition rate shows the nanoparticle diffusion into a thin cell wall having many lipopolysaccharides and a few peptidoglycan layers.

The mechanism involved in the antibacterial activity of Fe-SnO<sub>2</sub> NPs is assumed to be influenced by the generated reactive oxygen species, viz., H<sub>2</sub>O<sub>2</sub>, superoxide, and hydroxyl radicals, which will penetrate through the bacterial cell membrane, damage DNA, and protein, which will finally inhibit bacterial growth. For Fe-SnO<sub>2</sub> NPs, the increased antibacterial action can be attributed to their smaller particle size, as evidenced by XRD and FESEM analysis, which leads to the generation of a large number of reactive oxygen species on the surface of bacterial cells, resulting in intracellular component leakage and cell death [32, 33]. To check the reliability of the obtained results, a triplicate of the experiment is carried out. Similar types of enhancement in antibacterial activity of doped SnO<sub>2</sub> NPs have been reported previously by Manjula and Selvan and Amutha et al. [34, 35].

## 4. Conclusion

Pure and Fe-SnO<sub>2</sub> NPs at different molar concentrations are synthesized by the hydrothermal method. The structural studies confirmed the successful incorporation of Fe ions into the Sn lattice of SnO<sub>2</sub> NPs without the formation of any other secondary phases. SEM micrographs revealed the formation of irregularly shaped particles with agglomeration. EDS analysis confirmed the presence of Fe, Sn, and O as major trace elements. The PL emission peaks seen in the visible region confirm the presence of intrinsic defects such as oxygen vacancies and tin interstitials. H<sub>2</sub>O<sub>2</sub>-assisted photocatalytic degradation of crystal violet dye using Fe-SnO<sub>2</sub> NPs has shown increased efficiency with the increase of Fe-dopant concentration, and a maximum efficiency of 98% was observed for 0.05 M Fe-SnO<sub>2</sub> NPs. The radical scavenger studies indicated that the holes and superoxide radicals played major roles while the hydroxide radicals played a relatively minor role in the degradation process. The investigations on the role of pH of the dye solution revealed a maximum degradation efficiency when the pH value is 10. The synthesized Fe-SnO<sub>2</sub> NPs showed excellent stability and almost constant dye degradation efficiency even after 5 cycles when reused. The antibacterial activity of Fe-SnO<sub>2</sub> NPs investigated against gram-negative *Escherichia coli* by using the colony count method shown the promising potential of the synthesized nanoparticles as antibacterial agents.

## Data Availability

Data are available upon reasonable request by the corresponding author.

## Conflicts of Interest

The authors declare that they have no conflicts of interest.

## Acknowledgments

The UGC-DAE-CSR (project sanction no.: CSR-KN/CRS-107/2018–19/1046) is acknowledged for funding to carry out this research. We also acknowledge the SRMIST's HRTEM Facility support from MNRE, Government of India (project no. 31/03/2014-15/PVSE-R&D).

## References

- [1] S. K. Tammina, B. K. Mandal, and N. K. Kadiyala, "Photocatalytic degradation of methylene blue dye by nonconventional synthesized SnO<sub>2</sub> nanoparticles," *Environmental Nanotechnology, Monitoring & Management*, vol. 10, pp. 339–350, 2018.
- [2] M. Chauhan, N. Kaur, P. Bansal, R. Kumar, S. Srinivasan, and G. R. Chaudhary, "Proficient photocatalytic and sonocatalytic degradation of organic pollutants using CuO nanoparticles," *Journal of Nanomaterials*, vol. 2020, Article ID 6123178, 15 pages, 2020.
- [3] N. M. Mahmoodi, F. Najafi, and A. Neshat, "Poly (amido-amine-co-acrylic acid) copolymer: synthesis, characterization and dye removal ability," *Industrial Crops and Products*, vol. 42, pp. 119–125, 2013.
- [4] N. M. Mahmoodi, A. Taghizadeh, M. Taghizadeh, and M. Azimi, "Surface modified montmorillonite with cationic surfactants: preparation, characterization, and dye adsorption from aqueous solution," *Journal of Environmental Chemical Engineering*, vol. 7, no. 4, article 103243, 2019.
- [5] B. Hayati, N. M. Mahmoodi, and A. Maleki, "Dendrimer-titanium nanocomposite: synthesis and dye-removal capacity," *Research on Chemical Intermediates*, vol. 41, no. 6, pp. 3743–3757, 2015.
- [6] N. M. Mahmoodi and M. H. S. Dastgerdi, "Clean laccase immobilized nanobiocatalysts (graphene oxide - zeolite nanocomposites): from production to detailed biocatalytic degradation of organic pollutant," *Applied Catalysis B: Environmental*, vol. 268, article 118443, 2020.
- [7] N. M. Mahmoodi, "Synthesis of magnetic carbon nanotube and photocatalytic dye degradation ability," *Environmental Monitoring and Assessment*, vol. 186, no. 9, pp. 5595–5604, 2014.
- [8] M. Oveisi, M. A. Asli, and N. M. Mahmoodi, "Carbon nanotube based metal-organic framework nanocomposites: synthesis and their photocatalytic activity for decolorization of colored wastewater," *Inorganica Chimica Acta*, vol. 487, pp. 169–176, 2019.
- [9] N. M. Mahmoodi, M. Oveisi, M. Bakhtiari et al., "Environmentally friendly ultrasound-assisted synthesis of magnetic zeolitic imidazolate framework - graphene oxide nanocomposites and pollutant removal from water," *Journal of Molecular Liquids*, vol. 282, pp. 115–130, 2019.
- [10] N. M. Mahmoodi, M. Bashiri, and S. J. Moeen, "Synthesis of nickel-zinc ferrite magnetic nanoparticle and dye degradation using photocatalytic ozonation," *Materials Research Bulletin*, vol. 47, no. 12, pp. 4403–4408, 2012.
- [11] A. A. A. Khalek, S. A. Mahmoud, and A. H. Zaki, "Visible light assisted photocatalytic degradation of crystal violet, bromophenol blue and eosin Y dyes using AgBr-ZnO nanocomposite," *Environmental Nanotechnology, Monitoring & Management*, vol. 9, pp. 164–173, 2018.
- [12] D. Chandran, L. S. Nair, S. Balachandran, and K. R. Babu, "Structural, optical, photocatalytic, and antimicrobial activities of cobalt-doped tin oxide nanoparticles," *Journal of Sol-Gel Science and Technology*, vol. 76, no. 3, pp. 582–591, 2015.
- [13] A. B. A. Baig, V. Rathinam, and V. Ramya, "Facile fabrication of Zn-doped SnO<sub>2</sub> nanoparticles for enhanced photocatalytic dye degradation performance under visible light exposure," *Advanced Composites and Hybrid Materials*, vol. 4, no. 1, pp. 114–126, 2021.
- [14] A. B. A. Baig, V. Rathinam, and J. Palaninathan, "Photodegradation activity of yttrium-doped SnO<sub>2</sub> nanoparticles against methylene blue dye and antibacterial effects," *Applied Water Science*, vol. 10, no. 2, 2020.
- [15] M. Sathishkumar and S. Geethalakshmi, "Enhanced photocatalytic and antibacterial activity of Cu:SnO<sub>2</sub> nanoparticles synthesized by microwave assisted method," *Materials Today*, vol. 20, pp. 54–63, 2020.
- [16] S. Ragupathy and T. Sathya, "Photocatalytic decolorization of brilliant green by Ni doped SnO<sub>2</sub> nanoparticles," *Journal of Materials Science: Materials in Electronics*, vol. 29, no. 10, pp. 8710–8719, 2018.
- [17] K. Sujatha, T. Seethalakshmi, A. P. Sudha, and O. L. Shanmugasundaram, "Photoluminescence properties of pure, Fe-doped and surfactant-assisted Fe-doped tin-oxide nanoparticles," *Bulletin of Materials Science*, vol. 43, no. 1, 2020.
- [18] M. Ghorbanpour and A. Feizi, "Iron-doped TiO<sub>2</sub> catalysts with photocatalytic activity," *Journal of Water and Environmental Nanotechnology*, vol. 4, no. 1, pp. 60–66, 2019.
- [19] A. B. A. Baig, V. Rathinam, and V. Ramya, "Synthesis and investigation of Fe doped SnO<sub>2</sub> nanoparticles for improved photocatalytic activity under visible light and antibacterial performances," *Materials and Technologies*, vol. 36, no. 10, pp. 623–635, 2021.
- [20] L. Segueni, A. Rahal, B. Benhaoua, N. Allag, A. Benhaoua, and M. S. Aida, "Iron doping SnO<sub>2</sub> thin films prepared by spray with moving nozzle: structural, morphological, optical, and type conductivities," *Digest Journal of Nanomaterials and Biostructures*, vol. 14, no. 4, pp. 923–934, 2019.
- [21] G. T. Rao, B. Babu, R. V. S. S. N. Ravikumar, J. Shim, and C. H. V. Reddy, "Structural and optical properties of Fe-doped SnO<sub>2</sub> quantum dots," *Materials Research Express*, vol. 4, no. 12, article 125021, 2017.
- [22] N. Ahmad, S. Khan, and M. M. N. Ansari, "Exploration of Raman spectroscopy, dielectric and magnetic properties of (Mn, Co) co-doped SnO<sub>2</sub> nanoparticles," *Physica B: Condensed Matter*, vol. 558, pp. 131–141, 2019.
- [23] S. Hussain, J. Jacob, N. Riaz et al., "Effect of growth temperature on catalyst free hydrothermal synthesis of crystalline SnO<sub>2</sub> micro-sheets," *Ceramics International*, vol. 45, no. 3, pp. 4053–4058, 2019.
- [24] S. Jayapandi, S. Premkumar, D. Lakshmi et al., "Reinforced photocatalytic reduction of SnO<sub>2</sub> nanoparticle by La incorporation for efficient photodegradation under visible light

- irradiation," *Journal of Materials Science: Materials in Electronics*, vol. 30, no. 9, pp. 8479–8492, 2019.
- [25] W. B. H. Othmen, B. Sieber, H. Elhouichet et al., "Effect of high Fe doping on Raman modes and optical properties of hydrothermally prepared SnO<sub>2</sub> nanoparticles," *Materials Science in Semiconductor Processing*, vol. 77, pp. 31–39, 2018.
- [26] Y. Bouznit and A. Henni, "Characterization of Sb doped SnO<sub>2</sub> films prepared by spray technique and their application to photocurrent generation," *Materials Chemistry and Physics*, vol. 233, pp. 242–248, 2019.
- [27] V. Kumar, A. Govind, and R. Nagarajan, "Optical and photocatalytic properties of heavily F<sup>-</sup>-Doped SnO<sub>2</sub> nanocrystals by a novel single-source precursor approach," *Inorganic Chemistry*, vol. 50, no. 12, pp. 5637–5645, 2011.
- [28] A. Ahmed, M. N. Siddique, T. Ali, and P. Tripathi, "Defect assisted improved room temperature ferromagnetism in Ce doped SnO<sub>2</sub> nanoparticles," *Applied Surface Science*, vol. 483, pp. 463–471, 2019.
- [29] S. Rahaman, M. Abushad, S. Naseem et al., "Unravelling the effect of Ni doping on the structural, optical and dielectric properties of nanocrystalline SnO<sub>2</sub>," *Chinese Journal of Chemical Physics*, vol. 66, pp. 543–552, 2020.
- [30] K. Karthik, V. Revathi, and T. Tatarchuk, "Microwave-assisted green synthesis of SnO<sub>2</sub> nanoparticles and their optical and photocatalytic properties," *Molecular Crystals and Liquid Crystals*, vol. 671, no. 1, pp. 17–23, 2018.
- [31] K. Tantubay and P. Das, "Hydrogen peroxide-assisted photocatalytic dye degradation over reduced graphene oxide integrated ZnCr<sub>2</sub>O<sub>4</sub> nanoparticles," in *Environmental Science and Pollution Research*, Springer, 2021.
- [32] Z. Obeizi, H. Benbouzid, T. Bouarroudj, and M. Bououdina, "Excellent antimicrobial and anti-biofilm activities of Fe-SnO<sub>2</sub> nanoparticles as promising antiseptics and disinfectants," *Advances in Natural Sciences: Nanoscience and Nanotechnology*, vol. 12, no. 1, article 015003, 2021.
- [33] S. M. Amininezhad, A. Rezvani, M. Amouheidari, S. M. Amininejad, and S. Rakhshani, "The antibacterial activity of SnO<sub>2</sub> nanoparticles against Escherichia coli and staphylococcus aureus," *Zahedan Journal of Research in Medical Sciences*, vol. 17, no. 9, article e1053, 2015.
- [34] N. Manjula and G. Selvan, "Magnetic and antibacterial properties of Zr-doped SnO<sub>2</sub> nanopowders," *Journal of Materials Science: Materials in Electronics*, vol. 28, no. 20, pp. 15056–15064, 2017.
- [35] T. Amutha, M. Rameshbabu, S. S. Florence, N. Senthilkumar, I. V. Potheher, and K. Prabha, "Studies on structural and optical properties of pure and transition metals (Ni, Fe and co-doped Ni-Fe) doped tin oxide (SnO<sub>2</sub>) nanoparticles for anti-microbial activity," *Research on Chemical Intermediates*, vol. 45, no. 4, pp. 1929–1941, 2019.